Multifrequency electrical impedance tomography with total variation regularisation

Zhou Zhou[1][2], Thomas Dowrick[2], Emma Malone[2], James Avery[2], Nan Li[1], Zhaolin Sun[1], Hui Xu[1] and David Holder[2]

[1]National University of Defense Technology, Changsha, 410073, P. R. China

[2]University College London, London, WC1E 6BT, UK

zhou.zhou.13@ucl.ac.uk

Abstract. Multifrequency Electrical Impedance Tomography (MFEIT) reconstructs the distribution of conductivity by exploiting the dependence of tissue conductivity on frequency. MFEIT can be performed on a single instance of data, making it promising for applications such as stroke and cancer imaging, where it is not possible to obtain a 'baseline' measurement of healthy tissue. A nonlinear MFEIT algorithm able to reconstruct the volume fraction distribution of tissue rather than conductivities has been developed previously. For each volume, the fraction of a certain tissue should be either 1 or 0; this implies that the sharp changes of the fractions, representing the boundaries of tissue, contain all the relevant information However, these boundaries are blurred by traditional regularisation methods employing l_2 norm. The Total Variation (TV) regularisation can overcome this problem, but it is difficult to solve due to its non-differentiability. As the fraction must be between 0 and 1, this imposes a constraint on the MFEIT method based on the fraction model. Therefore, a constrained optimisation method capable of dealing with non-differentiable problems is required. We propose a new constrained TV regularised method, to solve the fraction reconstruction problem, based on the Primal and Dual Interior Point Method (PDIPM) method. The noise performance of the new MFEIT method is analysed using simulations on a 2D cylindrical mesh. Convergence performance is also analysed, through experiments using a cylindrical tank. Finally, simulations on an anatomically realistic head-shaped mesh are demonstrated. The proposed MFEIT method with TV regularisation shows higher spatial resolution, particularly at the edges of the perturbation, and stronger noise robustness, and its image noise and shape error are 20% to 30% lower than the traditional fraction method.

Keywords: multifrequency electrical impedance tomography, total variation, fraction model

(Some figures may appear in colour only in the online journal)

1. Introduction

1.1. Background

MFEIT (Multifrequency Electrical Impedance Tomography) reconstructs the frequency dependent conductivity distribution within a body by measuring the surface voltages at different frequencies. Conventional EIT is typically the time difference application, where a baseline dataset is recorded and compared with a subsequent dataset recorded in the presence of some perturbations (Lionheart, 2003). However, this is not appropriate for a number of medical applications, such as acute stroke, brain injury and breast cancer (Holder, 2004), since patients are admitted after disease onset and therefore the baseline measurements of healthy tissue are unavailable (Romsauerova *et al.,* 2006). As such, MFEIT offers a potential solution, as images can be produced from data collected at a single given point in time. However, MFEIT application is more challenging due to the high sensitivity of its solution to modelling and instrumentation errors (Kolehmainen *et al.,* 1997; McEwan *et al.,* 2007; Malone *et al.,* 2014b) .

1.1.1. MFEIT Methods. The absolute imaging method (Yerworth *et al.,* 2004), simple frequency-difference method and WFD method (Weighted Frequency Difference) (Ahn *et al*., 2011) have previously been proposed as solutions to the inverse problem of MFEIT. Absolute imaging is theoretically possible, but is computationally intensive and very sensitive to errors resulting from inaccurate boundary geometry, electrode positions and other sources of systematic artefacts in measured data (McEwan *et al.,* 2007; Seo *et al.,* 2008). The simple frequency-difference method, which reconstructs the EIT images from relative data referred to a certain frequency using a linear method, was proven that it can work in a homogeneous and frequency invariant background (Packham *et al.,* 2012). WFD has been proven that it can reconstruct a perturbation in a frequency variant background (Seo *et al.,* 2008, Jun *et al.,* 2009a, Ahn *et al.,* 2011), but as a linear algorithm its application is restricted by the availability of linearised approximation (Jun *et al.,* 2009). For example, WFD cannot reconstruct proper images if the area of perturbation is too large (Malone *et al*., 2014b). A method for performing MFEIT using Spectral Constraints (MFEITSC) was proposed by Malone *et al*., (2014b, 2014a). The inverse problem was modified by substituting the conductivity with the volume fraction of each tissue in each voxel, describing the physical distribution of tissues in the domain. The newly reconstructed parameter, referred to 'fraction' in this paper, is independent of frequency, so the data acquired at all frequencies can be processed simultaneously, and frequency independent modelling errors can be significantly reduced (Malone *et al.,* 2014b). This method allows for the quantitative recovery of tissue fraction values by a non-linear reconstruction method. This approach differs significantly from linear techniques, and does not require frequency weighting such as that employed in WFD imaging (Malone et al., 2014b).

1.1.2. Motivation. In addition to the property of frequency-independence, the fractions have another significant characteristic, which has not yet been properly and appropriately considered. In theory, for a sufficiently fine mesh, the fraction in each voxel should be either zero or one, regardless of the conductivity contrast between the background and perturbation. Thus, the boundaries of the fraction reconstructions have high contrast (0 for background and 1 for perturbations). Even for a coarse mesh, the voxels with fraction values between 0 and 1 are few, since the range of the physical boundaries is usually small, so the property of high contrast is retained. Existing implementations of the fraction model using MRF (Markov Random Field) regularisation (Malone *et al.*, 2014b) blur the boundaries, as they adopt the l_2 norm to smooth sharp changes. The commonly used Tikhonov regularisation techniques also produce a smooth solution, due to the inclusion of the l_2 norm. This smoothing effect, which can be mitigated by the l_1 regularisation technique, leads to further deterioration in the inherently low spatial resolution of EIT. The values of the fractions are restricted between 0 and 1, which transforms the corresponding inverse problem into a constrained optimisation problem. Consequently, a novel method that can solve the constrained optimisation while preserving sharp changes would be advantageous.

1.1.3. Introduction to regularisation with Total Variation. One regularisation technique that does not cause smoothing of boundaries is the total variation (TV) regularisation technique. TV is a popular regularisation method; it has been applied to different imaging modalities and can preserve sharp discontinuities in an image while removing noise and other unwanted details (Rudin *et al*., 1992;Chan &Wong, 1998; Vogel & Oman, 1996; 1998). The ability of TV to preserve edges in reconstructed images is due to its usage of the l_1 norm penalty term, which is not differentiable at every point. This differentiability means that traditional derivative-based methods usually used for solving regularised problems are not available.

Only a small number of publications have considered using the TV technique for EIT (Borsic *et al.,* 2010; Chung *et al.,* 2005; Jung & Yun, 2014). Borsic *et al.* (2010) used the Primal Dual Interior Point Method (PDIPM) to solve the TV regularised problem of time difference EIT. They showed that the algorithm works well in simulations and for *in vivo* experimental lung ventilation data. Recently, Jung and Yun (2014) proposed a first-order TV method, Linearised Alternating Direction Method of Multipliers (LADMM), and demonstrated that it has a similar resolution to PDIPM in small meshes. LADMM requires many more iterations to converge in comparison with PDIPM, due to the exclusion of second order derivative (Jung & Yun 2014). Thus, the methodology is not suitable for nonlinear applications, because the nonlinear inverse problem requires calculations of the Jacobian matrix and line search for each iteration, which are computationally intensive.

1.2. Purpose
The purpose of this paper is to propose a new MFEIT algorithm based on TV regularisation, which combines a novel constrained TV regularised algorithm and the fraction model. Its performance in respect to resolution, noise robustness and convergence rate will be evaluated. Specifically, the following questions will be explored:
(1) What are the advantages and disadvantages of this novel algorithm?
(2) Is this novel algorithm promising for MFEIT application to brain function imaging?

1.3. Experimental design
Experiments were undertaken using two algorithms: the existing fraction algorithm (Malone *et al.,* 2014b), and the aforementioned novel TV regularised fraction algorithm. First, a simulation using a cylindrical model was considered, using different noise levels to test the noise performance of the algorithms. Then, experiments in a cylindrical tank were carried out to verify that the new algorithm works in relation to real data. Last, an anatomically realistic head-shaped model, including skull and scalp, was used to evaluate the potential of the algorithm on EIT of brain function.

2. Methods

2.1. General considerations

2.1.1. Forward problem
The forward problem involves the determination of boundary voltages, given the internal conductivity distribution of the object and the Neumann boundary conditions. The forward problem can be solved analytically only in cases of very simple geometries. Therefore the finite element method was employed to solve the forward problem. The discretisation for Finite Element Method (FEM) was performed in custom written software (Aristovich *et al.,* 2014). All considered meshes were quality-checked in accordance with the Joe-Liu quality measure (Liu & Joe 1994), with the quality parameter being >0.9 for 99.99% voxels.

2.1.2. Inverse solution

The inverse problem determines the internal conductivity distribution of an object from a set of measured boundary voltages for a given injected current. As the inverse problem of EIT applications is severely ill-posed, a penalty term, based on prior knowledge, is always introduced:

$$\min_{\boldsymbol{\sigma}} \ (\| \mathbf{V} - A(\boldsymbol{\sigma}) \|^2 + \lambda \| R(\boldsymbol{\sigma}) \|) \qquad (1)$$

where $\mathbf{V}$ represents the boundary voltages, $\boldsymbol{\sigma}$ denotes the conductivities, A is the forward operator, λ represents the regularisation parameter, $R(\boldsymbol{\sigma})$ is the regularisation term. The regularisation matrix is commonly of the form of an identity matrix, partial differentiable matrix or diagonal matrix.

2.1.3. Fraction model

The existing fraction MFEIT algorithm implements spectral constraints (Malone *et al.,* 2014b), which means that the conductivities of each tissue must be known for all measurement frequencies. Therefore, for all frequencies $\{ \omega_i ; i=1 , \dots , M \}$ and tissues $\{ t_j ; j=1 , \dots , T \}$, we have

$$\varepsilon_{ij} = \sigma^{t_j}(\omega_i) \qquad (2)$$

where ε_{ij} is the conductivity of tissue t_j on the frequency ω_i.

The conductivity $\sigma_n(\omega_i)$ of the nth voxel at a certain frequency ω_i can be modelled as the linear combination of the conductivities of individual tissue fractions:

$$\sigma_n(\omega_i) = \sum_{j=1}^{T} f_{nj} \varepsilon_{ij} \qquad (3)$$

where f_{nj} denotes the fraction of the tissue t_j in the nth voxel. The fractions, independent of frequency, represent the physical distribution of tissues for each voxel, so it meets the following constraints:

$$0 \leq f_{nj} \leq 1$$
$$\sum_{j=1}^{T} f_{nj} = 1 \qquad (4)$$

The objective minimisation problem consists of both inequality constraints $0 \leq f_{nj} \leq 1, j=1 , \dots , T$ and equality constraints $\sum_{j=1}^{T} f_{nj} = 1$ as (4), which can be further simplified. The equality constraints $\sum_{j=1}^{T} f_{nj} = 1$ are enforced by substituting $f_{n1} = 1 - \sum_{j=2}^{T} f_{nj}$. Therefore, the constraints in (4) are equivalent to the inequality constraints $0 \leq f_{nj} \leq 1, j=2 , \dots , T$, and the remaining fraction is cacluated by $f_{n1} = 1 - \sum_{j=2}^{T} f_{nj}$.

The minimisation problem of EIT (1) is expressed in terms of the fractions by substituting the conductivities with (3):

$$\min_{\mathbf{f}} (\| \mathbf{V}(\omega_i) - A(\sum_{j=1}^{T} \mathbf{f}_j \varepsilon_{ij}) \|^2 + \lambda \| G(\mathbf{F}) \|) \qquad (5)$$

where $\mathbf{f}_j = \{ f_{nj} ; n=1 , \dots , N \}$, $\mathbf{F} = \{ \mathbf{f}_j ; j=1 , \dots , T \}$ and N denotes the number of voxels, G is the regularisation term for $\mathbf{F}$.

In order to remove the frequency independent modelling error and additive noise, relative data, referred to the data of a frequency ω_0, is processed. The minimisation problem for relative data is shown as:

$$H(\mathbf{f}) = \min_{\mathbf{f}} (\| (\mathbf{V}(\omega_i) - \mathbf{V}(\omega_0)) - (A(\sum_{j=1}^{T} \mathbf{f}_j \varepsilon_{ij}) - A(\sum_{j=1}^{T} \mathbf{f}_j \varepsilon_{0j})) \|^2 + \lambda \| G(\mathbf{F}) \|) \qquad (6)$$

where ε_{0j} is the conductivity value of tissue t_j on the frequency ω_0. The fractions are reconstructed simultaneously for all tissues at all frequencies, and the constraints of the fractions $0 \le f_{nj} \le 1$, $j=2, \dots, T$, are imposed so that it becomes a constrained minimisation problem.

The Jacobian matrix $\mathbf{J}_{\omega_i}(\mathbf{f}_j)$ for the fractions of the freqency ω_i is obtained by using the chain rule,

$$\mathbf{J}_{\omega_i}(\mathbf{f}_j) = \frac{\partial A(\boldsymbol{\sigma}_i)}{\partial \mathbf{f}_j} = \frac{\partial A(\boldsymbol{\sigma}_i)}{\partial \boldsymbol{\sigma}_i}\frac{\partial \boldsymbol{\sigma}_i}{\partial \mathbf{f}_j} = \mathbf{J}(\boldsymbol{\sigma}_i)\varepsilon_{ij} \tag{7}$$

2.1.4. Total variation regularisation term

The l_2 norm is commonly used in the regularisation term, but this biases the solution to the minimisation problem towards a smoother solution. The total variation regularisation adopts the l_1 norm, which does not penalise image discontinuities. Consequently, the TV regularisation technique is particularly attractive for reconstructing sharp transitions. For a differentiable function on a domain Ω the total variation is (Rudin *et al.,* 1992; Holder, 2004)

$$TV(\boldsymbol{\sigma}) = \int_\Omega |\nabla\boldsymbol{\sigma}| \tag{8}$$

The introduction of the l_1 norm makes the inverse problem non-differentiable, so the traditional gradient class inversion algorithms are not available.

2.1.5. PDIPM for EIT

PDIPM, an unconstrained optimisation method, has been proposed to address the EIT inverse problem with TV regularisation (Borsic *et al.,* 2010). The basic idea underlying PDIPM is the conversion of non-differentiable problems into equivalent differentiable problems by introducing dual variables and the corresponding dual problem (Borsic *et al,.* 2010; Borsic & Adler, 2012; Fan & Wang, 2010; Mamatjan *et al.,* 2013).

The original minimisation problem with the TV regularisation term (8) is labelled the 'primal' problem. Dual variables $\boldsymbol{\chi}$, a vector of scalar auxiliary variables, are introduced to the primal problem according to the Cauchy-Schwartz inequality.

$$\max_{|\boldsymbol{\chi}| \le 1} \min_{\boldsymbol{\sigma}} (\| \mathbf{V} - A(\boldsymbol{\sigma}) \|^2 + \lambda\boldsymbol{\chi}^T\mathbf{L}\boldsymbol{\sigma}) \tag{9}$$

where $\mathbf{L}$ denotes the TV regularisation matrix and λ represents the regularisation parameter. This constrained maximisation problem, called the dual problem, is differentiable but still difficult to solve, due to the box constraints of the dual variables.

The primal and dual problems have the same optimal solution, which can be found by nulling the difference between the primal and dual problems. The primal-dual gap problem is:

$$\| \mathbf{L}\boldsymbol{\sigma} \| - \boldsymbol{\chi}^T\mathbf{L}\boldsymbol{\sigma} = \mathbf{0} \tag{10}$$

A smoothness parameter $\beta > 0$ is introduced to (10) to obtain differentiability by replacing $\| \mathbf{L}\boldsymbol{\sigma} \|$ with $\sqrt{\| \mathbf{L}\boldsymbol{\sigma} \|^2 + \beta}$.

The PDIPM framework is constructed by combining the dual problem and the primal-dual gap problem, and solve these using a multi-variable Guass Newton method. The final form is:

$$\delta\boldsymbol{\sigma} = -[\mathbf{J}^T\mathbf{J} + \lambda\mathbf{L}^T\mathbf{E}^{-1}\mathbf{K}\mathbf{L}]^{-1} \cdot [\mathbf{J}^T(\mathbf{V} - A(\boldsymbol{\sigma})) + \lambda\mathbf{L}^T\mathbf{E}^{-1}\mathbf{L}\boldsymbol{\sigma}]$$

$$\mathbf{E} = diag(\sqrt{|\mathbf{L}_i\boldsymbol{\sigma}|^2 + \beta}) \quad \mathbf{K} = \mathbf{I} - \mathbf{E}^{-1}diag(\chi_i\mathbf{L}_i\boldsymbol{\sigma}) \tag{11}$$

$$\delta\boldsymbol{\chi} = -\boldsymbol{\chi} + \mathbf{E}^{-1}\mathbf{L}\boldsymbol{\sigma} + \mathbf{E}^{-1}\mathbf{K}\mathbf{L}\delta\boldsymbol{\sigma}$$

where $\mathbf{L}_i$ is the i row of $\mathbf{L}$, and χ_i is the ith element of the dual variables $\boldsymbol{\chi}$.

Typically, the primal variables **σ** are updated using a precise gradient-based algorithm, and the dual variables **χ** are updated typically using a simple, computationally easier, method, such as the scaling rule (Anderson *et al.,* 1998).

2.2. A constrained total variation algorithm for EIT

The constrained total variation algorithm method, MFEIT using Total Variation (MFEITTV), is made up of two steps (Nocedal *et al.,* 1999). The first step is to optimise the objective function (6) in the bounded constraints $0 \le f_{nj} \le 1, j=2, \dots, T; n=1, \dots, N,$ and the second step is to apply unconstrained optimisation. The optimisation solution of the first step is called Cauchy point, which is obtained using the steepest descent method in the feasible region.

We convert the matrix $f_{nj}, j=2, \dots, T; n=1, \dots, N,$ to vector $f_l, l=1, \dots, N \times (T-1)$, for the convenience of the calculation.

2.2.1. Finding the Cauchy point

In order to find the Cauchy point, we first search along the negative gradient direction from the initial point. When an upper or lower bound is met, the search direction is projected onto the constraint. The Cauchy point is obtained by examing each of the line segments that make up $f_l, l=1, \dots, N \times (T-1),$. To perform this search, the values of step sizes $s_l^*, l=1, \dots, N \times (T-1)$, where the corners of the search path occur, require to be determined:

$$s_l^* = \begin{cases} (f_l - 1)/g_l & if \ g_l < 0 \\ (f_l - 0)/g_l & if \ g_l > 0 \\ \infty & otherwise \end{cases} \quad (12)$$

where $\{ g_l ; l=1, \dots, N \times (T-1) \}$ denotes the gradient direction. After removing the duplicate values and zero values of s_l^*, we sort the remaining values into an ordered sequence and examine the intervals $[0, s_1], [s_2, s_3] \dots$ in turn. Assuming the step size s of the minimiser is in the interval of $[s_k, s_{k+1}]$, we have:

$$\begin{aligned} \mathbf{f} &= \mathbf{f}_k + \Delta s \mathbf{p}_k, \\ \Delta s &= s - s_k, \\ \Delta s &\in [0, s_{k+1} - s_k], \\ \mathbf{p} &= -\mathbf{g} \end{aligned} \quad (13)$$

where $\mathbf{g} = \{ g_l ; l=1, \dots, N \times (T-1) \}$ denotes the gradient direction. For other intervals such as $[s_{k-1}, s_k]$, $\mathbf{f}$ is updated by $\mathbf{f} = \mathbf{f}_k + s_k \mathbf{p}_k$ after we find $\Delta s \notin [0, s_k - s_{k-1}]$. Δs is calculated by substituting $\mathbf{f}$ with $\mathbf{f}_k + \Delta s \mathbf{p}_k$, and then objective function is converted to the quadratic form $M_k + M_k' \Delta s + M_k'' (\Delta s)^2$ along each straight section of the search path, after expanding and grouping the coefficients M_k, M_k' and M_k'' of $1, \Delta s, (\Delta s)^2$. The minimum of the quadratic function is obtained by differentiating with repsect to Δs. If $\Delta s' \in [0, s_{k+1} - s_k)$ and $M_k'' > 0$, the minimiser, called the Cauchy point, is identified at $s = s_k + \Delta s'$. Otherwise, the Cauchy point is at $s = s_k$ when $M_k' > 0$.

2.2.2. Updating the primal variable

For those voxels beyond the boundaries of the constrained area, they are marked and will not be involved into the following process. The Newton-Krylov method (Horesh *et al.,* 2007) is employed to find the search direction of updating the primal variables with the initial point of the Cauchy point. The step size is determined using the Brent line-search method with a gold-section bracketing loop

(Brent, 1973; Ziegel *et al.,* 2007). The values of all optimal fractions cannot be guaranteed to satisfy the box constraints, as the solution is found by using unconstrained optimisation. Thus, the constraints must be enforced using

$$f_l = \begin{cases} 0 & if \ f_l \leq 0 \\ 1 & if \ f_l \geq 1 \\ f_l \ otherwise \end{cases} \tag{14}$$

2.2.3. Updating the dual variable

According to (11), the dual variable is updated thus:

$$\delta\boldsymbol{\chi} = -\boldsymbol{\chi} + \mathbf{E}^{-1}\mathbf{L}\boldsymbol{\sigma} + \mathbf{E}^{-1}\mathbf{K}\mathbf{L}\delta\mathbf{f} \tag{15}$$

The scaling length rule (Andersen *et al.,* 1999), as shown in (16), is introduced to find the step size of the dual variables, as a traditional line search approach is not guaranteed to reveal an ascent direction for the dual objective function (11) (Borsic *et al.,* 2010).

$$\boldsymbol{\chi}_{p+1} = \boldsymbol{\chi}_p + \min(1, \varphi^*)\delta\boldsymbol{\chi}$$
$$\varphi^* = \sup\{\varphi : |\boldsymbol{\chi}_p + \varphi\delta\boldsymbol{\chi}| \leq 1\} \tag{16}$$

where $\boldsymbol{\chi}_p$ are the dual variables of the *p*th iteration.

The iteration stop criterion is checked after updaing the dual variable. The overall procedure is demonstrated in the flow chart shown in figure 1.

2.2.4. Newton-Krylov method

The commonly used Gaussian Newton method, with the form of $\partial\boldsymbol{\sigma} = (\mathbf{J}^T\mathbf{J})^{-1}\mathbf{J}\partial V$, is not suitable for the large-scale problems, because the matrix $(\mathbf{J}^T\mathbf{J})^{-1}$ with size $N \times N$, where *N* denotes the number of voxels of the mesh, is impractical for storing or processing when *N* is very large. Consequently, the Krylov subspace method is introduced, with the form of $\mathbf{J}^T(\mathbf{J}\partial\boldsymbol{\sigma}) = \mathbf{J}\partial V$. This iterative method has been proven to have a short calculation time even for a large mesh, as the mesh $(\mathbf{J}^T\mathbf{J})$ with size $N \times N$ does not appear during calculation (Horesh *et al.,* 2007).

2.2.5. Iteration stop criterion

An iteration-terminating criterion was adopted based on the relative decrease of the objective function, and the iterative algorithms were stopped when the relative decrease of this function was less than 1%.

$$[\frac{H(\mathbf{f}_{p+1})}{H(\mathbf{f}_p)} - 1] \leq 0.01 \tag{17}$$

where $H(\mathbf{f}_p)$ is the value of the objective function of the *p*th iteration as shown in (6).
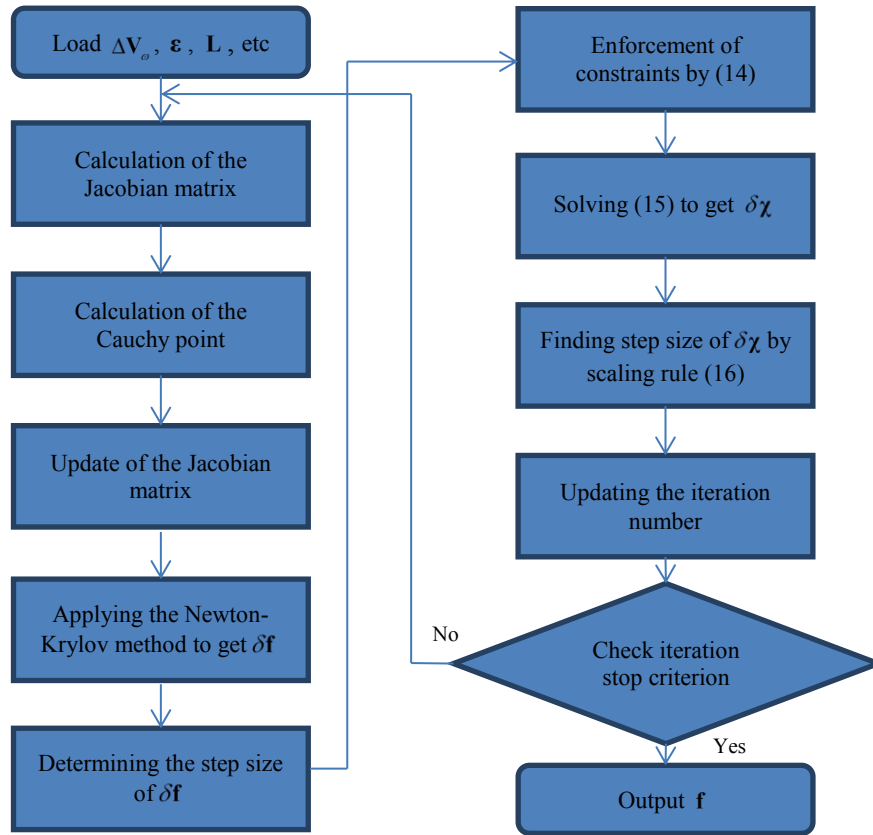
Figure 1. The flow chart of the proposed algorithm.

2.2.6. Parameter selection

The performance of the inverse problem algorithm is affected by the regularisation parameter, and some regularisation parameter selection methods, such as the cross-validation, L curve and discrepancy method, have been used in EIT. In this instance, the nonlinear L curve method (Hansen & O'Leary, 1993) is adopted to compare the proposed fraction algorithm and the conventional fraction algorithm, as the cross-validation method is computationally intensive and the prior knowledge of a noise model is not known.

The smoothness parameter, transforming the original non-differentiable problem to a differentiable approximation, should be a small value. However, the algorithm may diverge if this parameter is too small. In the present study, the initial value of this parameter was set as 1e-4, and divided by 2 for each iteration.

2.3. Experimental setup

2.3.1. Cylindrical simulated model and tank

Simulations were made in a cylindrical mesh, with a diameter of 19 cm and height of 10 cm, with 62784 voxels and a ring of 32 electrodes, 1 cm in diameter, evenly placed at a height of 5 cm, and a 33rd ground electrode on the base of the mesh in the centre. A current of peak amplitude 133 μA at 640 Hz, 654 kHz, 1.024 MHz and 1.3 MHz was injected through polar electrodes. The voltages on all adjacent pairs of electrodes not involved in delivering the current were recorded, for a total of 448 measurements per frequency. A simulated potato perturbation with a diameter of 4cm was placed in (-4 cm 0 cm 0 cm), where the origin was the centre of mesh (figure 2). To study the noise performance,

Gaussian white noise was added to the simulated boundary voltage, with a Signal to Noise Ratio (SNR) of 60 dB, 40 dB and 30 dB.

Experimental recordings were made in a cylindrical Perspex tank with the same dimensions and design as the mesh above. Electrodes were made of stainless steel. The boundary voltages of four output frequencies were measured using the UCLH Mk 2.5 system (McEwan *et al.,* 2006) and averaged over 10 frames. A potato cylinder with diameter 4.6 cm and length 10 cm was placed into a suspension of carrot cubes, approximately 4mm along each edge, in 0.1% NaCl saline at two locations, 4cm either side of the centre. The tank experiments were undertaken at room temperture.

2.3.2. Anatomically realistic 3D head-shaped model

An anatomically realistic 3D head-shaped model with three layers, corresponding to the scalp, skull and brain, was used, with 32 electrodes of diameter 10mm. The dimensions of the model were: height 16 cm; width 14 cm; depth 20 cm; and circumference 54 cm. The amplitude of the simulated injecting current was 140 μA and 12 frequencies were selected in the range of 5Hz - 5kHz, as suggested by Malone *et al*. (2014a). A fine mesh with 5 million voxels was used to simulate the boundary voltages, and a coarse mesh with 180 thousand voxels was used for reconstruction.

A spherical perturbation of diameter 3 cm was placed in posterior and lateral positions of brain, as shown in figures 8(a) (c), and the conductivity of the perturbation was set to match the reported values for ischaemic stroke (Malone *et al*., 2014a).

2.3.3. Tissue impedance spectra

Spectral information of the test tissues is required for the MFEIT algorithms of fractions. The biological test objects with frequency dependent conductivities were selected to simulate live tissues in cylindrical simulations and experiments. A mixture of carrot cubes of approximately 4 mm each side and a 0.1% concentration NaCl solution was used as the background medium. A potato cylinder with a diameter of 4.6 cm was placed in the carrot-saline mixture as a perturbation. In order to obtain the spectral values of the background and perturbation medium, the conductivities at 640 Hz, 654 kHz, 1.024 MHz and 1.3 MHz were measured, using a Hewlett-Packard 42847A impedance analyser (Hewlett-Packard, CA, USA) and Ag-AgCl electrodes, as the conductivity spectra of the two tissues in this range are distinctly different (Malone *et al*., 2014b) and correspond to the measurement frequencies of the UCLH MK 2.5 system. The carrot-saline and potato samples were measured using Perspex tubes of fixed diameter and two lengths. The electrode resistance was removed by plotting resistance against length and evaluating the offset of the line passing through the measurement points.

For the simulations of the human head, the conductivity spectra of the tissues (scalp, skull, brain, ischaemic, brain and blood) were taken from Romsauerova *et al*. (2006). Four frequencies were adopted in the range of 20 Hz - 3 kHz, as the conductivities in this range have the largest changes across frequencies (Malone *et al*., 2014a).

2.3.4. Image quantification

Image quality was assessed quantitatively according to three metrics (Fabrizi *et al.,* 2009). The information of the real perturbation is required to be known before quantifying images. The reconstructed perturbation is identified as the fractions of those voxels are larger than 0.3.

Image noise: inverse of the contrast-to-noise ratio between the perturbation P and background B

$$\frac{std(\mathbf{f}_B)}{|\bar{\mathbf{f}}_P - \bar{\mathbf{f}}_B|} \tag{18}$$

where $\bar{\mathbf{f}}_P$ and $\bar{\mathbf{f}}_B$ are the mean intensities of the perturbation and background and *std* is the standard deviation.

Localisation error: ratio between the norm of the *x-y-z* displacement of the centre of mass of the reconstructed perturbation P from the actual position (x, y, z), and the norm of the dimensions of the mesh (d_x, d_y, d_z).

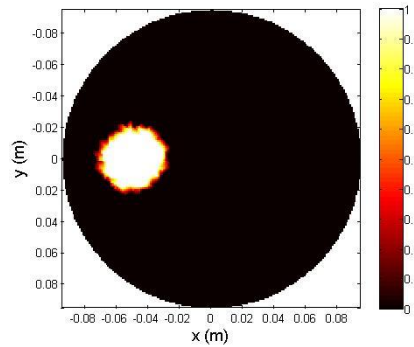$$\frac{\| \sum_{n \in P} \mathbf{f}_n(x_n, y_n, z_n) - (x, y, z) \|}{\| (d_x, d_y, d_z) \|} \tag{19}$$

where (x_n, y_n, z_n) denotes the position of the centre of the *n*th voxel.

Shape error: mean ratio of the difference between the dimensions of the simulated and reconstructed perturbations, respectively (l_x, l_y, l_z) and $(l_x^{'}, l_y^{'}, l_z^{'})$

$$\frac{1}{3}(\frac{|l_x - l_x^{'}|}{d_x} + \frac{|l_y - l_y^{'}|}{d_y} + \frac{|l_z - l_z^{'}|}{d_z}) \tag{20}$$
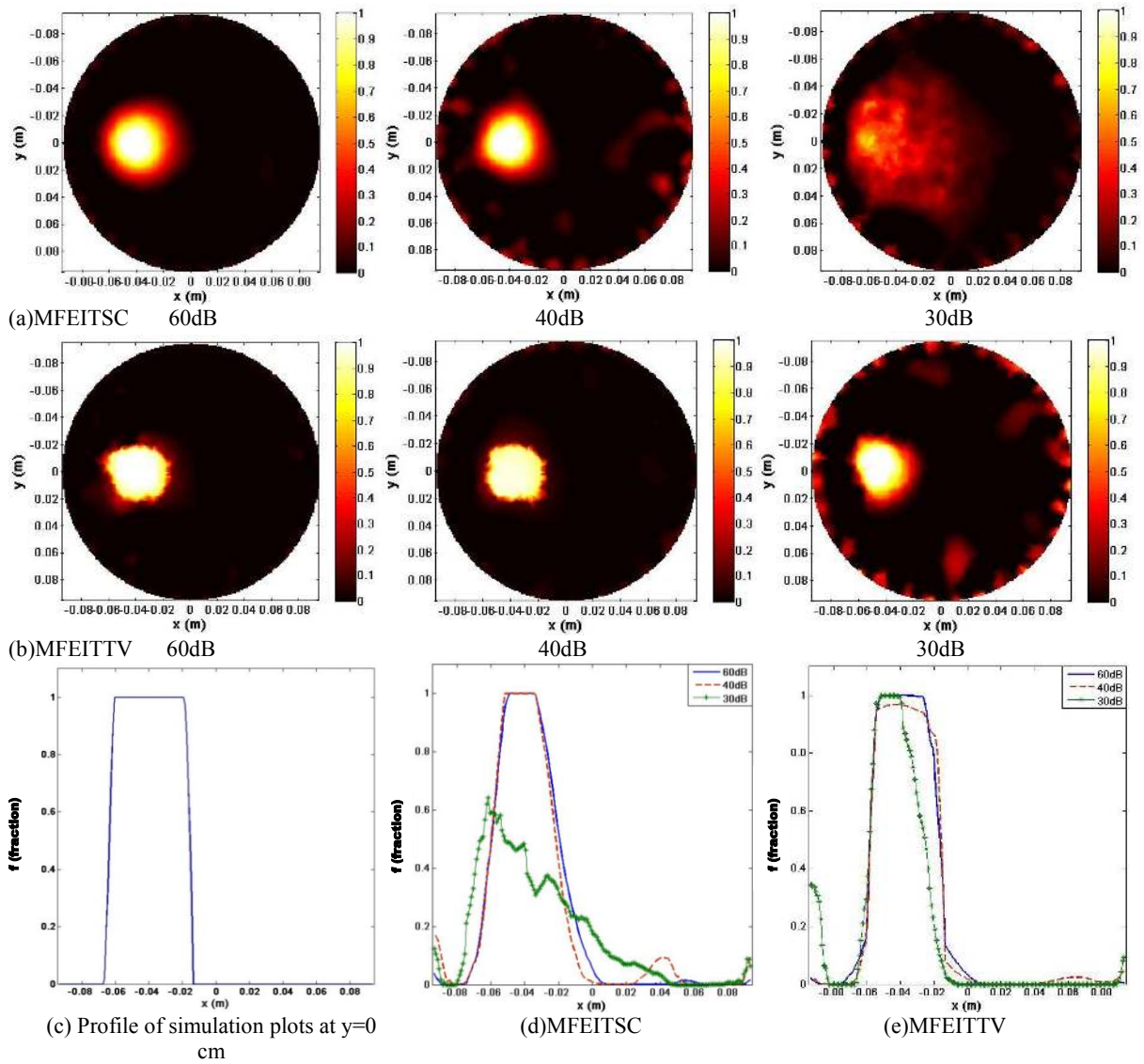
3. Results

3.1. Simulation

Figure 2. 2D simulation slice at *z*= 5 cm.

In the 2D simulation, across all noise levels, the MFEITTV correctly reconstructed the perturbation, while the MFEITSC did not produce an identifiable reconstruction when the SNR was at 30 dB (figure 3). It is shown that there are three distinct layers for reconstructed images of perturbations, with different colours from inside to out: white, yellow and orange for MFEITSC reconstructions of 60 dB and 40 dB, implying that the conductivity changes. In contrast, the reconstructed perturbations of MFEITTV have much thinner layers, which are difficult to identify. Therefore, the boundaries of all reconstructions for TV regularisation can be distinguished. The profiles in Figure 3(e) of 60dB and 40dB are close to the profile shown in Figure 3(c), though the interior boundaries of the image of SNR 30dB exhibit some blurring. As shown in Figure 3(d), the transient ranges representing the fraction decreases from 1 to 0 of MFEITSC are around 3 cm for 60dB and 40dB, while the transient ranges of MFEITTV are approximately 2 cm. Furthermore, the decreasing spatial slew rate of MFEITTV between fraction 1 and 0.2 is roughly five times larger than MFEITSC for 60dB and 40dB. For 30dB the MFEITSC's transient range of the inner side is larger than the radius of the mesh, 10cm, while MFEITTV has transient range smaller than 4cm. The MFEITTV profile in 30dB clearly demonstrates that the transient range is larger than in lower noise conditions, and the spatial slew rate of the inner side is slower than the outer side. The artefacts, representing the apparent conductivity changes unrelated to the perturbations, in the 40dB image of MFEITTV are fewer than in the image of MFEITSC. However, as illustrated in Figure 4(a), the new algorithm required 1~3 more iterations to converge compared with the traditional algorithm, across all noise levels. Convergence will be discussed further in the next section. Figure 4(b) demonstrated that MFEITTV has distinct lower image noises and shape errors than MFEITSC.
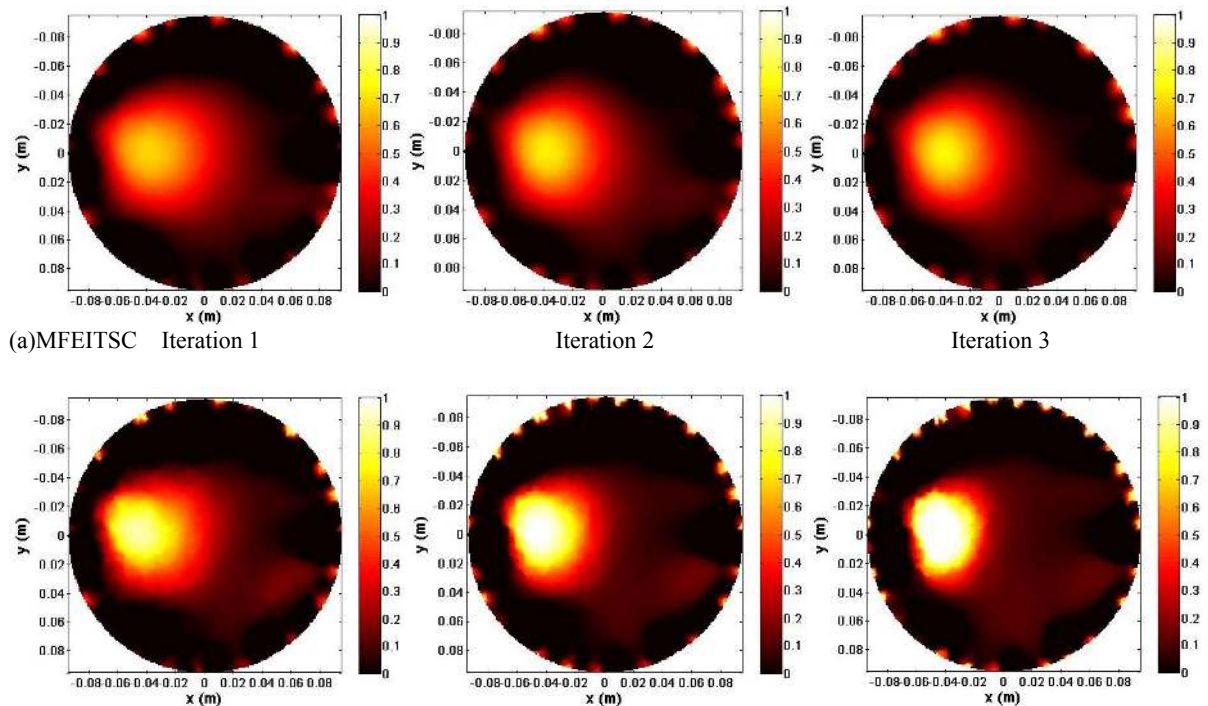
(a)MFEITSC 60dB   40dB   30dB

(b)MFEITTV 60dB   40dB   30dB

(c) Profile of simulation plots at y=0 cm (d)MFEITSC   (e)MFEITTV

Figure 3. Illustrations of the noise performance of the MFEITSC and MFEITTV of SNR 60dB, 40dB and 30dB: (a) 2D slices at z= 5cm of the MFEITSC, (b) 2D slices at z= 5cm of the MFEITTV, (c) profile at y= 0cm of the simulation, (d) profiles at y= 0cm of the MFEITSC, (e) profiles at y= 0cm of the MFEITTV.

(a)   (b)
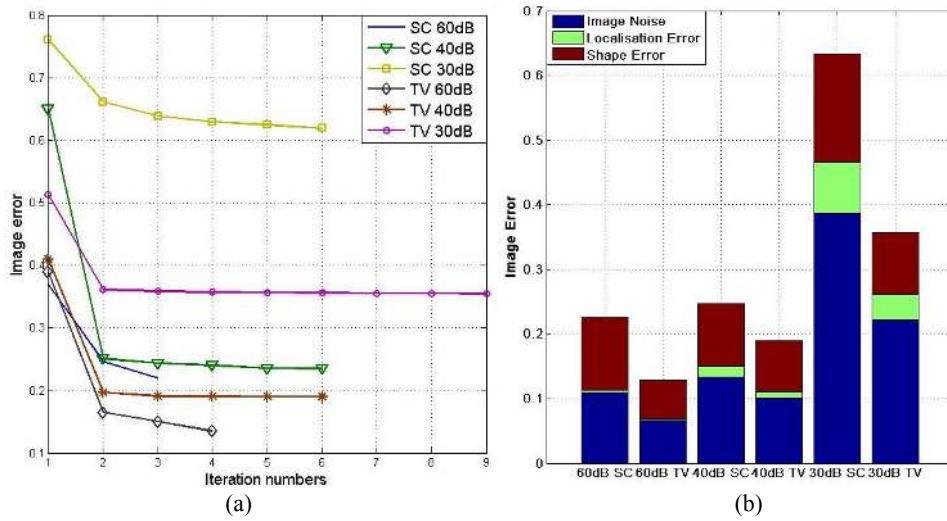
Figure 4. (a) Image error (sum of image noise, localisation error and shape error) changes as iterations(SC: MFEITSC; TV: MFEITTV), (b) image error for each algorithm (SC: MFEITSC; TV: MFEITTV) at all noise levels.
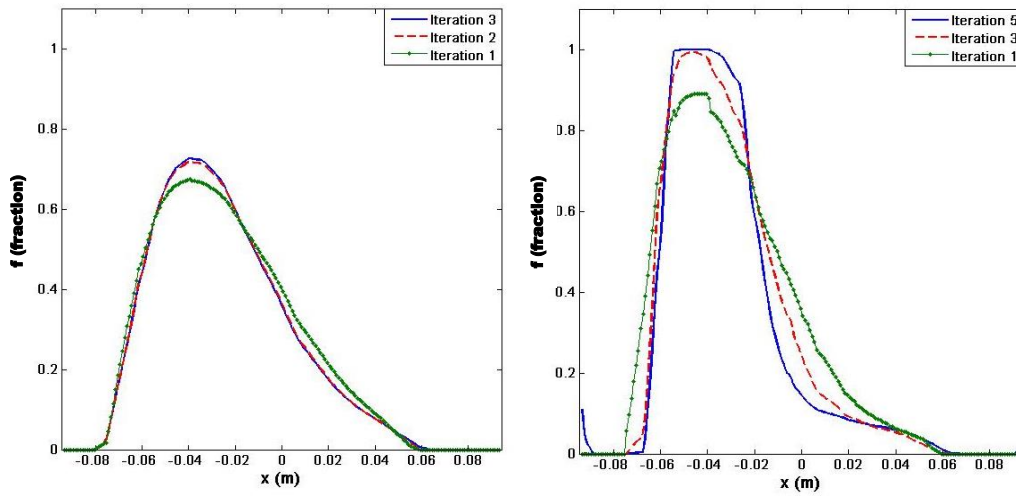
3.2. Cylindrical phantom study

For both locations of the perturbations of potato, the two methods can reconstruct the fraction distributions (Figure 5 & 6). The MFEITSC converged after three iterations, while the MFEITTV converged after five, as shown in Figure 5(c) (d) and Figure 6(c) (d). The new algorithm converged near to the minimum, after just two iterations; further iterations served to sharpen the boundary of the object, in iterations three to five, as shown in Figures 7(a). The relative decrease of objective function was 13% and 6% for iteration 1 to iteration 3, and iteration 3 to iteration 5 of MFEITTV, shown in Figure 5(d), and 14% and 6% in Figure 6(d). The image errors of the experiments were consistent with the simulations of noise robustness (Figure 7(b)).

(a)MFEITSC   Iteration 1   Iteration 2   Iteration 3

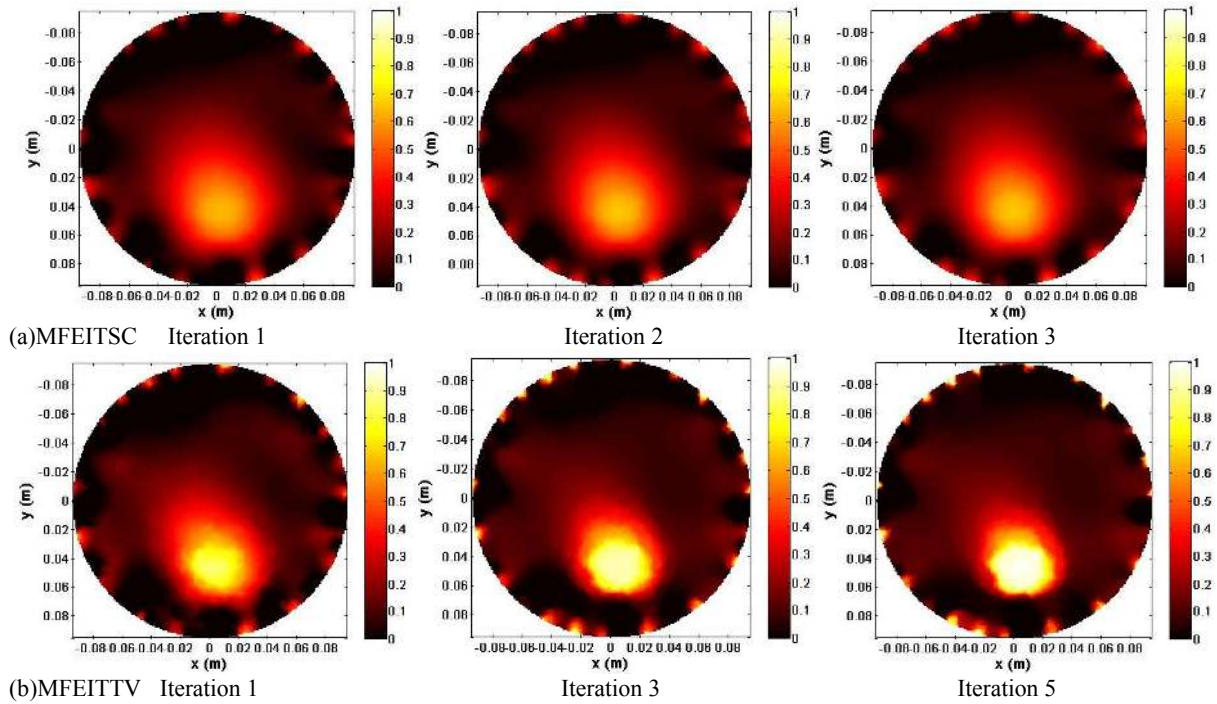Iteration 3   Iteration 5

(c)MFEITSC   (d)MFEITTV

Figure 5. Illustration of the reconstructions of the MFEITSC and MFEITTV for the cylindrical tank data of position 1. (a) 2D slice at z= 5cm for the MFEITSC, (b) 2D slice at z= 5cm for the MFEITTV (c) profile plots at y= 0cm for the MFEITSC, (d) profile plots at y= 0cm for the MFEITTV.

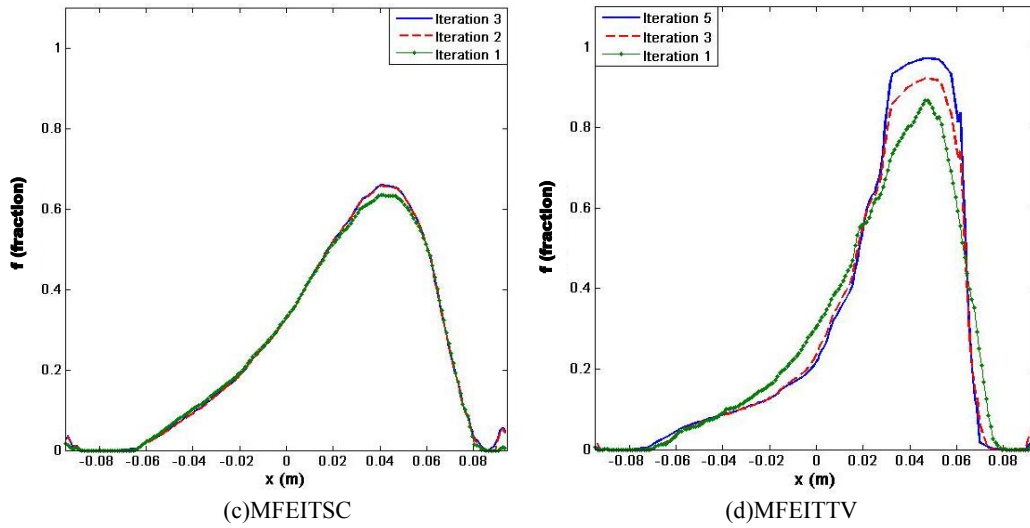(a)MFEITSC   Iteration 1   Iteration 2   Iteration 3

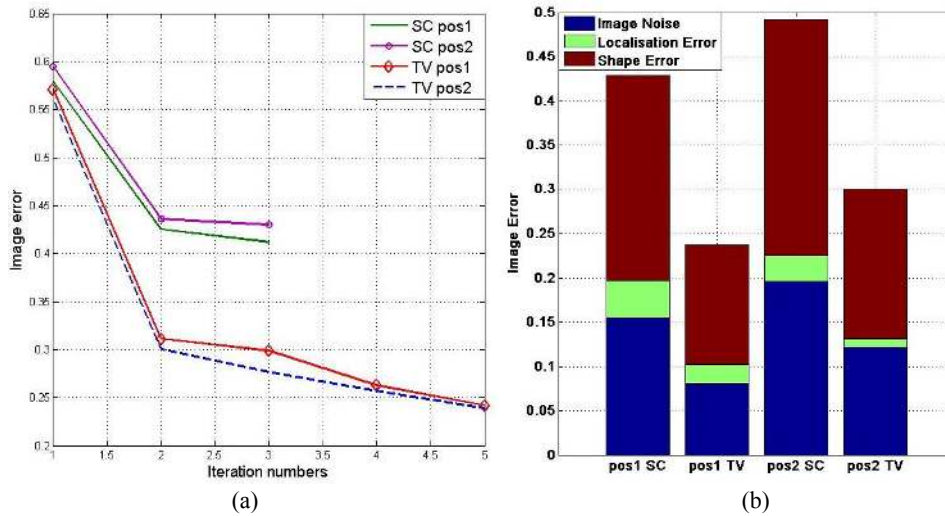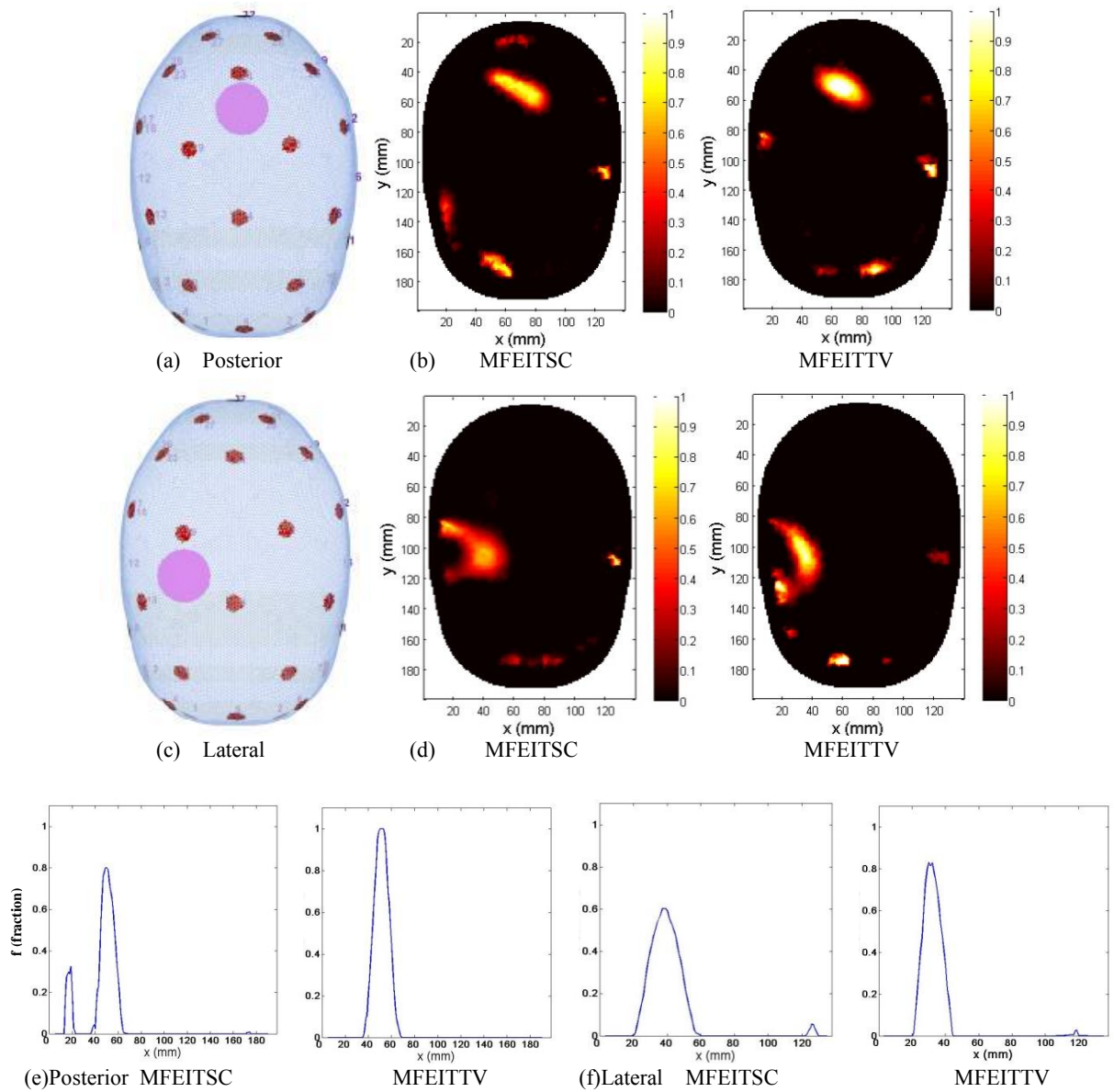(b)MFEITTV   Iteration 1   Iteration 3   Iteration 5

(c)MFEITSC   (d)MFEITTV

Figure 6. Illustration of the reconstructions of the MFEITSC and MFEITTV for the cylindrical tank data of position 2. (a) 2D slice at z= 5cm for the MFEITSC, (b) 2D slice at z= 5cm for the MFEITTV (c) profile plots at y= 0cm for the MFEITSC, (d) profile plots at y= 0cm for the MFEITTV.

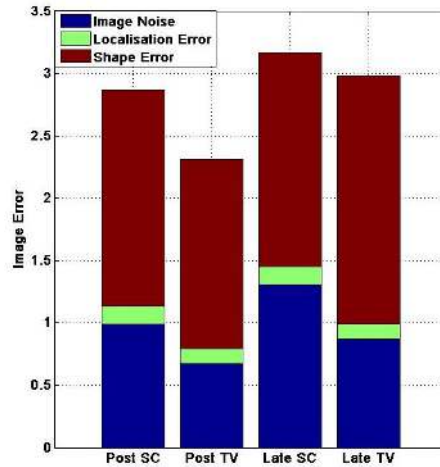(a)   (b)

Figure 7. (a) Image error (sum of image noise, localisation error and shape error) changes as iterations (SC: MFEITSC; TV: MFEITTV), (b) image error for each algorithm (SC: MFEITSC; TV: MFEITTV; pos: perturbation position) at all noise levels.

3.3. Anatomical head-shaped model simulation

The conductivity images reconstructed by MFEITTV, shown in Figure 8, demonstrate higher contrast, which is in agreement with the previous experiments and simulations. However, it is evident that neither algorithm can correctly reconstruct the shape of the perturbation. Additionally, more artefacts were generated in simulations of the human head than for previous cases. The image noises of MFEITTV were still lower than MFEITSC, but the shape error of MFEITTV of the lateral case was higher than corresponding reconstruction of MFEITSC (Figure 9).

(a) Posterior   (b) MFEITSC   MFEITTV

(c) Lateral   (d) MFEITSC   MFEITTV

(e)Posterior MFEITSC   MFEITTV   (f)Lateral MFEITSC   MFEITTV

Figure 8. Reconstructions of the MFEITSC and MFEITTV for the head shaped mesh: (a) simulated posterior stroke; (b) 2D slice of the posterior stroke; (c) simulated lateral stroke; (d) 2D slice of the lateral stroke; (e) profile of the y axis direction for the posterior stroke; (f) profile of the x axis direction for the lateral stroke.

Figure 9. Image error (sum of image noise, localisation error and shape error), for head-shaped model simulations (SC: MFEITSC; TV: MFEITTV; Post: posterior; Late: lateral).

4. Discussion

4.1. Summary of results

The findings are that the MFEITTV algorithm reconstructed the boundaries of perturbations better than the MFEITSC algorithm, for all noise levels. In MFEITSC images, the boundaries of perturbations were graded and presented gradually altered conductivity. The MFEITTV algorithm was superior in terms of noise robustness. The reconstructed image was unidentifiable for MFEITSC for 30dB SNR, and MFEITTV typically reconstructed fewer artefacts, clearly shown for 40dB SNR.

MFEITTV converged more slowly than MFEITSC in all conditions. MFEITTV required one more iteration for SNR of 60dB and three more for 30dB SNR. In the cylindrical phantom study and head simulations, however, MFEITTV demonstrated a slower convergence rate.

The tests in a cylindrical phantom and realistic head simulation revealed that MFEITTV is better able to preserve the boundaries of perturbations than is MFEITSC. The reconstructions of head simulations were less accurate and with more artefacts, due to the additional complexity of the skull and scalp.

4.2. Technical issues

During the study, the smoothness parameter was selected heuristically; however, superior results might be obtained by using a more optimised selection method, such as the cross-validation method. This is a substantial project, which is currently being undertaken, but is beyond the scope of this paper. In addition, the noise pattern added should be modified in future studies to simulate more realistic noise distribution. The performance of the proposed algorithm should also be considered in relation to errors of electrode position, contact impedance and mesh shape.

4.3. Assessment of the MFEITTV algorithm

The results reveal that the proposed TV algorithm yields improved spatial resolution, particularly in the reconstructions of the boundaries of the perturbation, obtained by the application of the l_1 norm. This advantage helps to determine the shapes and define the locations of perturbations, and is optimised when TV regularisation is applied to the reconstruction of fractions. A higher noise robustness of MFEITTV than MFEITSC is also demonstrated (figures 3 and 4(b)), and the transient range of high noise is wider than lower noise.

The convergence rate of the new method is slower than the traditional one (figures 4(a) and 7(a)). It is noted that PDIPM is iterative, even for linear applications, because it aims to solve the approximation rather than the real, non-differentiable problem (Borsic *et al*., 2010). Consequently, it is

likely that this iterative approach contributes to the slower convergence rate. Furthermore, the parameter selection becomes more complicated due to the introduction of the smoothness parameter, which is typically explored using the heuristic method.

The proposed algorithm is promising in relation to possible MFEIT application of imaging brain function. While the convergence rate is slower, the improvements in spatial resolution and noise robustness are significant enough to warrant its use.

5. Conclusions

In conclusion, a constrained TV inversion algorithm MFEITTV is proposed as the reconstruction method for the MFEIT problem using fraction model. The novel algorithm has better spatial resolution, particularly for the boundaries of perturbations, and superior noise robustness compared to the traditional algorithm. However, as stated, the convergence rate of MFEITTV is slower and the introduction of smoothness parameter complicates the parameter selection. Nevertheless, on balance, this algorithm is proven to be very promising for MFEIT of brain function.

Future work is required to investigate the automatic parameter selection method for MFEITTV method. The effect of the error of the conductivity spectral to the proposed algorithm's performance will be studied. We are also interested to research how to select the optimal frequency data as the reference. The proposed algorithm is planned to test in rat brain experiment.

Abbreviations

MFEIT: Multifrequency Electrical Impedance Tomography; TV: Total Variation; WFD: Weighted Frequency Difference; MFEITSC: MFEIT using Spectral Constraints; MRF: Markov Random Field; PDIPM: Primal Dual Interior Point Method; FEM: Finite Element Method; SNR: Signal to Noise Ratio; MFEITTV: MFEIT using Total Variation.

References

Ahn S, Oh T I, Jun S C, Seo J K and Woo E J 2011 Validation of weighted frequency-difference EIT using a three-dimensional hemisphere model and phantom. *Physiol. Meas.* **32** 1663–80 Online: http://www.ncbi.nlm.nih.gov/pubmed/21904022

Andersen K D, Christiansen E, Conn A R and Overton M L 1999 An Efficient Primal-Dual Interior-Point Method for Minimizing a Sum of Euclidean Norms *SIAM J. Sci. Comput.* Online: http://citeseerx.ist.psu.edu/viewdoc/summary?doi=10.1.1.46.555

Anderson K D, Christiansen E, Conn A R and Overton M L 1998 An Efficient Primal-Dual Interior-Point Method for Minimizing a Sum of Euclidean Norms Online: http://dl.acm.org/citation.cfm?id=890300

Aristovich K Y, dos Santos G S, Packham B C and Holder D S 2014 A method for reconstructing tomographic images of evoked neural activity with electrical impedance tomography using intracranial planar arrays. *Physiol. Meas.* **35** 1095–109 Online: http://stacks.iop.org/0967-3334/35/i=6/a=1095

Borsic A and Adler A 2012 A primal–dual interior-point framework for using the L1 or L2 norm on the data and regularization terms of inverse problems *Inverse Probl.* **28** 095011 Online: http://stacks.iop.org/0266-5611/28/i=9/a=095011

Borsic A, Graham B M, Adler A and Lionheart W R B 2010 In vivo impedance imaging with total variation regularization. *IEEE Trans. Med. Imaging* **29** 44–54 Online: http://www.ncbi.nlm.nih.gov/pubmed/20051330

Brent R P 1973 Algorithms for minimization without derivatives. Englewood Cliffs, New Jersey: Prentice-Hall Online: http://cds.cern.ch/record/113464

Chan T F and Wong C K 1998 Total variation blind deconvolution. *IEEE Trans. Image Process.* **7** 370–5 Online: http://www.ncbi.nlm.nih.gov/pubmed/18276257

Chung E T, Chan T F and Tai X-C 2005 Electrical impedance tomography using level set representation and total variational regularization *J. Comput. Phys.* **205** 357–72 Online: http://linkinghub.elsevier.com/retrieve/pii/S0021999104004711

Fabrizi L, McEwan A, Oh T, Woo E J and Holder D S 2009 An electrode addressing protocol for imaging brain function with electrical impedance tomography using a 16-channel semi-parallel system. *Physiol. Meas.* **30** S85–101 Online: http://iopscience.iop.org/0967-3334/30/6/S06

Fan W R and Wang H X 2010 3D modelling of the human thorax for ventilation distribution measured through electrical impedance tomography *Meas. Sci. Technol.* **21** 115801 Online: http://stacks.iop.org/0957-0233/21/i=11/a=115801

Hansen P C and O'Leary D P 1993 The Use of the L-Curve in the Regularization of Discrete Ill-Posed Problems *SIAM J. Sci. Comput.* **14** 1487–503 Online: http://epubs.siam.org/doi/abs/10.1137/0914086

Holder D S 2004 *Electrical Impedance Tomography: Methods, History and Applications* (CRC Press) Online: http://books.google.com/books?hl=en&lr=&id=cjcRd4m_jUQC&pgis=1

Horesh L, Schweiger M, Arridge S R and Holder D S 2007 Large-Scale Non-Linear 3D Reconstruction Algorithms for Electrical Impedance Tomography of the Human Head *World Congr. Med. Phys. Biomed. Eng. 2006 IFMBE Proc.* **14** 3862–5

Jun S C, Kuen J, Lee J, Woo E J, Holder D and Seo J K 2009a Frequency-difference EIT (fdEIT) using weighted difference and equivalent homogeneous admittivity: validation by simulation and tank experiment. *Physiol. Meas.* **30** 1087–99 Online: http://stacks.iop.org/0967-3334/30/i=10/a=009

Jun S C, Kuen J, Lee J, Woo E J, Holder D and Seo J K 2009b Frequency-difference EIT (fdEIT) using weighted difference and equivalent homogeneous admittivity: validation by simulation and tank experiment. *Physiol. Meas.* **30** 1087–99 Online: http://www.ncbi.nlm.nih.gov/pubmed/19738319

Jung Y M and Yun S 2014 Impedance Imaging with First Order TV Regularization. *IEEE Trans. Med. Imaging* Online: http://www.researchgate.net/publication/265094550_Impedance_Imaging_with_First_Order_TV_Regularization

Kolehmainen V, Vauhkonen M, Karjalainen P A and Kaipio J P 1997 Assessment of errors in static electrical impedance tomography with adjacent and trigonometric current patterns *Physiol. Meas.* **18** 289–303 Online: http://stacks.iop.org/0967-3334/18/i=4/a=003

Lionheart W R B 2003 EIT Reconstruction Algorithms: Pitfalls, Challenges and Recent Developments *Physiol. Meas.* Online: http://arxiv.org/abs/physics/0310151

Liu A and Joe B 1994 Relationship between tetrahedron shape measures *BIT* **34** 268–87 Online: http://link.springer.com/10.1007/BF01955874

Malone E, Jehl M, Arridge S, Betcke T and Holder D 2014a Stroke type differentiation using spectrally constrained multifrequency EIT: evaluation of feasibility in a realistic head model. *Physiol. Meas.* **35** 1051–66 Online: http://www.ncbi.nlm.nih.gov/pubmed/24844796

Malone E, Sato Dos Santos G, Holder D and Arridge S 2014b Multifrequency electrical impedance tomography using spectral constraints. *IEEE Trans. Med. Imaging* **33** 340–50 Online: http://www.ncbi.nlm.nih.gov/pubmed/24122550

Mamatjan Y, Borsic A, Gürsoy D and Adler A 2013 An experimental clinical evaluation of EIT imaging with ℓ1 data and image norms. *Physiol. Meas.* **34** 1027–39 Online: http://stacks.iop.org/0967-3334/34/i=9/a=1027

McEwan A, Cusick G and Holder D S 2007 A review of errors in multi-frequency EIT instrumentation. *Physiol. Meas.* **28** S197–215 Online: http://stacks.iop.org/0967-3334/28/i=7/a=S15

McEwan A, Romsauerova A, Yerworth R, Horesh L, Bayford R and Holder D 2006 Design and calibration of a compact multi-frequency EIT system for acute stroke imaging. *Physiol. Meas.* **27** S199–210 Online: http://iopscience.iop.org/0967-3334/27/5/S17

Nocedal J, Wright S J and Robinson S M 1999 *Numerical Optimization* (Springer Science & Business Media) Online: http://books.google.co.uk/books/about/Numerical_Optimization.html?id=epc5fX0lqRIC&pgis=1

Packham B, Koo H, Romsauerova A, Ahn S, McEwan A, Jun S C and Holder D S 2012 Comparison of frequency difference reconstruction algorithms for the detection of acute stroke using EIT in a realistic head-shaped tank. *Physiol. Meas.* **33** 767–86 Online: http://iopscience.iop.org/0967-3334/33/5/767/article/

Romsauerova A, McEwan A, Horesh L, Yerworth R, Bayford R H and Holder D S 2006 Multi-frequency electrical impedance tomography (EIT) of the adult human head: initial findings in brain tumours, arteriovenous malformations and chronic stroke, development of an analysis method and calibration. *Physiol. Meas.* **27** S147–61 Online: http://www.ncbi.nlm.nih.gov/pubmed/16636407

Rudin L I, Osher S and Fatemi E 1992 Nonlinear total variation based noise removal algorithms *Phys. D Nonlinear Phenom.* **60** 259–68 Online: http://www.sciencedirect.com/science/article/pii/016727899290242F

Seo J K, Lee J, Kim S W, Zribi H and Woo E J 2008 Frequency-difference electrical impedance tomography (fdEIT): algorithm development and feasibility study. *Physiol. Meas.* **29** 929–44 Online: http://www.ncbi.nlm.nih.gov/pubmed/18603667

Vogel C R and Oman M E 1998 Fast, robust total variation-based reconstruction of noisy, blurred images. *IEEE Trans. Image Process.* **7** 813–24 Online: http://www.ncbi.nlm.nih.gov/pubmed/18276295

Vogel C R and Oman M E 1996 Iterative Methods for Total Variation Denoising *SIAM J. Sci. Comput.* **17** 227–38 Online: http://epubs.siam.org/doi/abs/10.1137/0917016

Yerworth R J, Horesh L, Bayford R, Tizzard A and Holder D S 2004 Robustness of linear and nonlinear reconstruction algorithms for brain EITS. Online: https://eprints.mdx.ac.uk/2925/

Ziegel E, Press W, Flannery B, Teukolsky S and Vetterling W 2007 *Numerical Recipes 3rd Edition: The Art of Scientific Computing* (Cambridge University Press) Online: https://books.google.com/books?hl=en&lr=&id=1aAOdzK3FegC&pgis=1